Investigation of Structure, Ionic Conductivity, and Electrochemical Stability of Halogen Substitution in Solid-State Ion Conductor $Li_3YBr_xCl_{6-x}$

Van Der Maas, Eveline; Zhao, Wenxuan; Cheng, Zhu; Famprikis, Theodosios; Thijs, Michel; Parnell, Steven R.; Ganapathy, Swapna; Wagemaker, Marnix

DOI
10.1021/acs.jpcc.2c07910

Publication date
2022

Document Version
Final published version

Published in
Journal of Physical Chemistry C

THE JOURNAL OF PHYSICAL CHEMISTRY C
A JOURNAL OF THE AMERICAN CHEMICAL SOCIETY

pubs.acs.org/JPCC Article

Investigation of Structure, Ionic Conductivity, and Electrochemical Stability of Halogen Substitution in Solid-State Ion Conductor $Li_3YBr_xCl_{6-x}$

Eveline van der Maas,[†] Wenxuan Zhao,[†] Zhu Cheng, Theodosios Famprikis, Michel Thijs, Steven R. Parnell, Swapna Ganapathy,* and Marnix Wagemaker*

Cite This: https://doi.org/10.1021/acs.jpcc.2c07910 Read Online

ABSTRACT: Li_3YX_6 (X = Cl, Br) materials are Li-ion conductors that can be used as solid electrolytes in all solid-state batteries. Solid electrolytes ideally have high ionic conductivity and (electro)chemical compatibility with the electrodes. It was proven that introducing Br to Li_3YCl_6 increases ionic conductivity but, according to thermodynamic calculations, should also reduce oxidative stability. In this paper, the trade-off between ionic conductivity and electrochemical stability in $Li_3YBr_xCl_{6-x}$ halogen-substituted compounds is investigated. The compositions of $Li_3YBr_{1.5}Cl_{4.5}$ and $Li_3YBr_{4.5}Cl_{1.5}$ are reported for the first time, along with a consistent analysis of the whole $Li_3YBr_xCl_{6-x}$ (x = 0−6) tie-line. The results show that, while Br-rich materials are more conductive (5.36×10^{-3} S/cm at 30 °C for x = 4.5), the oxidative stability is lower (~3 V compared to ~3.5 V). Small Br content (x = 1.5) does not affect oxidative stability but substantially increases ionic conductivity compared to pristine Li_3YCl_6 (2.1 compared to 0.049×10^{-3} S/cm at 30 °C). This work highlights that optimization of substitutions in the anion framework provide prolific and rational avenues for tailoring the properties of solid electrolytes.

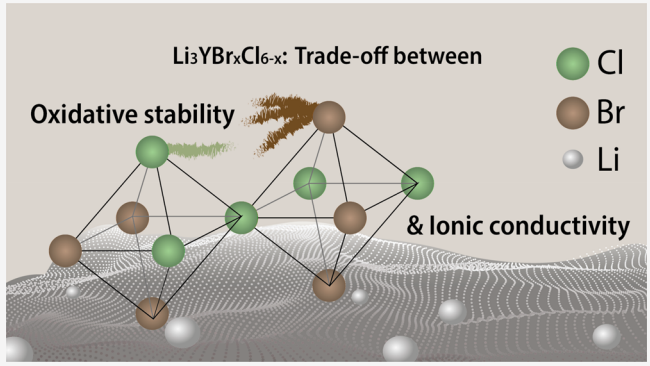

■ INTRODUCTION

Solid-state electrolytes for all-solid-state batteries (ASSBs) have been intensively researched in recent years, due to the improved safety they offer compared to liquid electrolytes and because they may enable alternative electrodes.[1] In 2018, Asano et al.[2] reported that the ternary halides Li_3YCl_6 and Li_3YBr_6 have ionic conductivities of ~1×10^{-3} S/cm and showcased ASSBs with Coulombic efficiencies of 94% using (uncoated) $LiCoO_2$ as the active material in the cathode composite. Since then, the material family $Li_3M(III)X_6$ (M(III) = Y, In, Sc, lanthanides; X = Cl, Br, I)) and other halide solid electrolytes have gained renewed interest in the scientific community due to their favorable combination of ionic conductivity (~mS/cm) and high-voltage cathode compatibility.[3−6] More recently, Zhou et al.[7] reached a milestone in the development of ASSBs using a $Li_2In_xSc_{0.66-x}Cl_4$ electrolyte. The ASSB with this electrolyte possessing a 2×10^{-3} S/cm ionic conductivity and a 4.7×10^{-10} S/cm electronic conductivity, reached 3000 cycles at 80% capacity retention when cycled between 2.8−4.3 V vs Li/Li^+ using $LiNi_{0.85}Co_{0.1}Mn_{0.05}O_2$ as the cathode (6.21 mg/cm^2) at 3C.[7] Considering these promising results, further improvements and fundamental understanding of such electrolytes may accelerate the development of practical ASSBs.

A strategy that has been successfully employed to tune the ionic conductivity of $Li_3M(III)X_6$ materials is halogen substitution.[8−13] Specifically for the compositional tie-line between Li_3YCl_6 and Li_3YBr_6, the $Li_3YBr_3Cl_3$ composition was shown to have a 7.2×10^{-3} S/cm ionic conductivity at room temperature (compared to the ~1×10^{-3} S/cm of the end members Li_3YCl_6/Li_3YBr_6 ref 2). Based on thermodynamic phase equilibrium calculations, it has been predicted that Li_3YCl_6 should be stable between 0.62 and 4.21 V vs Li/Li^+ and Li_3YBr_6 between 0.59 and 3.15 V vs Li/Li^+ (ref 14). According to these calculations, the materials would decompose into the YX_3 precursor and the halogen gas X_2 at high potentials (oxidation) and to metallic Y and LiX (X = Cl, Br) at low potentials (reduction). These calculations suggest that introducing Br may reduce the high-voltage stability, leading to a trade-off between cathode compatibility and ionic

Received: November 10, 2022
Revised: November 29, 2022
Published: December 16, 2022

conductivity. However, it has been shown that such calculations do not always reflect the practically relevant stability window of solid electrolytes, as the (possible) formation of intermediate phases are not considered.[15]

More generally, it has been proposed that the reduction and oxidation potential of the solid electrolyte upon lithiation/delithiation is a more accurate measure of the practical electrochemical stability window because the energetics of the reaction intermediates and non-equilibrium states are captured.[15] The stability window based on the oxidation and reduction potentials was found to be larger compared to thermodynamic calculations and matched the experimentally measured oxidation and reduction voltages for argyrodite-type Li_6PS_5Cl, garnet-type $Li_7La_3Zr_2O_{12}$, and NASICON-type $Li_{1.5}Al_{0.5}Ge_{1.5}(PO_4)_3$ (ref 15). For Li_3YBr_6, this method proposes a stability window between 0 and 3.43 V vs Li/Li^+ (ref 16) (compared to the previously predicted window of 0.59−3.15 V vs Li/Li^+). For Li_3YCl_6, no data simulated data using this method isavailable.

Specifically for $Li_3M(III)Cl_6$ (M(III) = Bi, Dy, Er, Ho, In, Lu, Sc, Sm, Tb, Tl, Tm, Y), the influence of the M(III) in different chlorides on the high-voltage stability was calculated to be between 4.26 and 4.38 V, with the majority at 4.26 V vs Li/Li^+ (ref 17). Recent experimental results showed that the difference in the high-voltage stability between solid-electrolytes with different M(III)/M(IV) is larger than expected in some cases, and that not only the electrochemical stability is relevant in such systems, but also the stability against oxygen release especially in combination with high capacity $LiNi_{0.85}Co_{0.1}Mn_{0.05}O_2$ (ref 18).

In this study, we report an experimental study of the substitution series $Li_3YBr_xCl_{6-x}$ (x = [0, 6] steps of 1.5) and investigate the influence of the halogen composition on the crystal structure, ionic conductivity, and the electrochemical stability window. It is found that the composition $Li_3YBr_xCl_{6-x}$ (x = 1.5) is a good compromise, with increased ionic conductivity compared to Li_3YCl_6 while maintaining the higher oxidative stability of Li_3YCl_6 compared to the bromide end-member.

METHODS

Synthesis of Halide SSEs. For the ampule synthesis of $Li_3YBr_xCl_{6-x}$, stoichiometric mixtures of the precursors ($x \leq 3$: LiCl (>99%, Sigma-Aldrich), LiBr (>99.99%, Sigma-Aldrich), YCl_3(99.99%, Sigma-Aldrich); $x > 3$: LiCl, LiBr, YBr_3(99.9% REO)) were filled in quartz ampules in an argon-filled glovebox. Then the ampules were evacuated and refilled to 200 mbar argon, flame-sealed, and placed in a muffle furnace. The powder mixtures were heated to 650 °C (above their melting point) in 4 h, held at that temperature for 24 h, and then cooled down to room temperature over 24 h. The resulting products were pulverized using pestle and mortar until a fine powder was obtained. The mechanochemical synthesis of $Li_3YBr_xCl_{6-x}$ with x = 3 was carried out by ball milling of precursors (YCl_3 and LiBr in a molar ratio of 1:3). Each 45 mL ZrO_2 ball mill jar (Fritsch) was filled with a total amount of 3 g of material with 20 g of Φ3 mm and 60 g of Φ10 mm ZrO_2 balls as milling media and tightly closed in the glovebox. The milling was conducted for 288 cycles of 5 min (each followed by 5 min rest) with a rotation speed of 500 rpm. After every 2 h, the mixtures were homogenized in the argon-filled box by scraping off the material pressed to the wall. A small part of the resulting material was taken out every 4 h for analysis. The as-milled products were subsequently put in the furnace for a sequential crystallization. The annealing was performed in quartz ampules in the same way as described above, at a temperature of 200−600 °C for 5 h with a heating rate of 2 °C per minute. The ampules were naturally cooled down to room temperature after annealing.

X-ray Diffraction. The samples were analyzed using a X'Pert-Pro diffractometer (PANalytical) equipped with a Cu Kα radiation (λ = 1.5406 Å) source operating at 45 kV and 40 mA. The samples were prepared by filling the powder into an airtight holder, which consisted of a silicon zero-diffraction wafer separated from the environment with a Kapton film arch. The data were collected at room temperature and atmospheric pressure by scanning over the 2θ range of 10 to 90°. The measured X-ray diffraction patterns were analyzed by Le Bail refinement using GSAS-II.[19,20]

Neutron Diffraction. Neutron diffraction was performed on the PEARL[21] diffractometer of the Reactor Institute Delft at a wavelength of 1.667 Å. The sample was filled in 7 mm diameter vanadium cans, which were filled in an argon-filled glovebox and sealed using rubber O-rings.

Rietveld Refinement. Rietveld refinement of the neutron diffraction data was performed using GSAS-II.[36,37] For the monoclinic phase, Y and Li were found to occupy the same crystallographic site. Due to the opposite sign coherent scattering length of these atoms (b_{Li} = −1.90 fm, b_Y = 7.75 fm), this led to a diminution of the signal intensity. As the full occupancy of the site is also not known, it was not possible to automatically refine this ratio due to divergence of the fit. Therefore, the refinement was done manually trying out (almost) all possible configurations, and deciding on the best fit based on visual inspection and the goodness of fit. Due to this difficulty, no conclusions have been drawn in this report on the differences between the occupancy parameters extracted. Crystal structures were visualized in VESTA.[22]

AC Impedance. AC impedance spectroscopy was used to determine the ionic conductivity of the synthesized powders. A homemade cell was used consisting of an insulating alumina hollow cylinder with two stainless steel plungers that are used both to initially compress the powder into a pellet and act as current collectors. The cell was assembled in an Ar-filled glovebox by filling 100 mg of powder into the alumina cylinder (inner diameter of Φ10 mm) and cold-pressing the powder into a pellet (392 MPa) using the steel plungers. The assembly was screwed tight under pressure using three (electronically insulated) screws. The measurements were performed on an Autolab electrochemical workstation (AUT86298) in a frequency range between 1 MHz and 100 Hz. The obtained data were fit using the commercial software RelaxIS (rhd instruments). The datasets were fit using a L-R-CPE circuit, which was validated by the Kramers−Kronig relations (see supporting files). The values of the parameter fits were used to calculate the ionic conductivities and the Arrhenius relationship. The error of individual conductivity measurements was calculated from Gaussian error propagation as proposed by Krasnikova et al.:[23]

$$\mathrm{RSD}_\sigma = \frac{\Delta\sigma}{\sigma} = \sqrt{\left(\frac{\Delta l}{l}\right)^2 + \left(\frac{\Delta R}{R}\right)^2 + \left(\frac{\Delta A}{A}\right)^2}$$

considering the influence of pellet thickness l and the error of the fit of the resistance R. Due to the nature of the setup, the error in the area, A, is considered negligible by the authors. A

https://doi.org/10.1021/acs.jpcc.2c07910
J. Phys. Chem. C XXXX, XXX, XXX−XXX

5% error was estimated for the pellet thickness (from the standard deviation of the thickness measured by the micrometer at different positions across the pellet), due to deviations in the thickness across the pellet. The error of the activation energy was calculated based on the fit of the Arrhenius relationship.

Electrochemical Measurements. The redox activity of the solid electrolytes was measured in the same assembly as the ionic conductivity, consisting of an alumina cylinder and stainless steel plungers.

The solid electrolyte−carbon composites were made by ball milling of the solid electrolytes with Super C45 and carbon nanofibers in the weight ratio of 0.85:0.10:0.05 for 2 h at 300 rpm. This mixture was tested for both oxidation and reduction stability. Depending on the reaction, either a lithium source or drain is needed as the counter electrode with a known constant potential.

Lithium titanate ($Li_4Ti_5O_{12}$, from altair nano) was used as a lithium drain. As the material does not have a constant potential at the beginning of the lithiation, the material was prelithiated chemically using *n*-butyllithium (1.6 M from Merck Sigma). The amount of *n*-butyllithium needed to half lithiate the $Li_4Ti_5O_{12}$ to $Li_{5.5}Ti_5O_{12}$ (prelithiated LTO) was calculated, and the reaction was carried out in hexane while stirring continuously inside an Ar-filled glovebox. After the reaction, the hexane was evaporated. For the measurements, the prelithiated LTO, the $Li_3YBr_xCl_{6-x}$ solid electrolyte, Super C45, and carbon nanofibers were ball milled with the ratio of 0.45:0.40:0.10:0.05 for 2 h at 300 rpm. Twenty-five milligrams of that mixture was used as the electrode.

As a lithium source, Li−In alloy was used. A Φ7 mm indium foil (∼58 mg) was prelithated with Φ3 mm Li foil (∼1 mg) by pressing the foils on top of each other. Li in indium is at 0.62 V vs Li/Li^+, and therefore, the in foil will lithiate spontaneously.

The fabrication of ASSBs starts with a cold pressing of 150 mg of the $Li_3YBr_xCl_{6-x}$ solid electrolytes under the pressure of 392 MPa. Sequentially, 16 mg of the halide−carbon mixture was placed and pressed under the pressure of 490 MPa on the one side, and the reference electrodes were then pressed on the other side (prelithiated LTO and In−Li alloy under the pressure of 490 and 50 MPa, respectively).

The oxidation and reduction voltages were measured by drawing a constant current of 6.5 $\mu A/cm^2$ to 0 V vs Li/Li^+ (reduction of the solid electrolyte), i.e., galvanostatically charging to 3.5 V versus prelithiated LTO or discharging to −0.62 V versus the In−Li alloy with a current density of 6.5 $\mu A/cm^2$. For the determination of the electrochemical stability window, the differential capacity was calculated based on the charge and discharge profiles.

Battery Assembly. ASSBs were assembled using single crystal NCM 811 (MSE supplies) as a cathode and Li−In as an anode. To ensure reversibility on the anode side, argyrodite Li_6PS_5Cl (acquired from NEI corporation) was used as an interlayer between the halide SE and the Li−In alloy. During assembly, the first 50 mg of the halide solid electrolyte was pressed at 20 MPa for 2 min. Then 50 mg of argyrodite was added on the other side and the pressing repeated. Around 10 mg of NCM 811 (composite 70% NCM 811 and 30% halide solid electrolyte, mixed using pestle and mortar) was added on the halide SE side. Prelithiated In foil (52 mg of indium foil, 8 mm diameter, and 2 mg of Li-metal foil pressed on) was then added on the argyrodite Li_6PS_5Cl side. The whole cell was pressed at 5 MPa for 1 min. The cells were cycled at C/10 between 2.75 and 4.3 V vs Li/Li^+.

RESULTS AND DISCUSSION

A series of $Li_3YBr_xCl_{6-x}$ (x = [0, 6] steps of 1.5) solid electrolytes were synthesized by direct co-melting of the precursors in evacuated silica ampules at 650 °C. The powders obtained were phase-pure for all compositions. The X-ray diffraction patterns shown in Figure 1a clearly show that the materials crystallize in two different phases, depending on the ratio between Cl and Br.

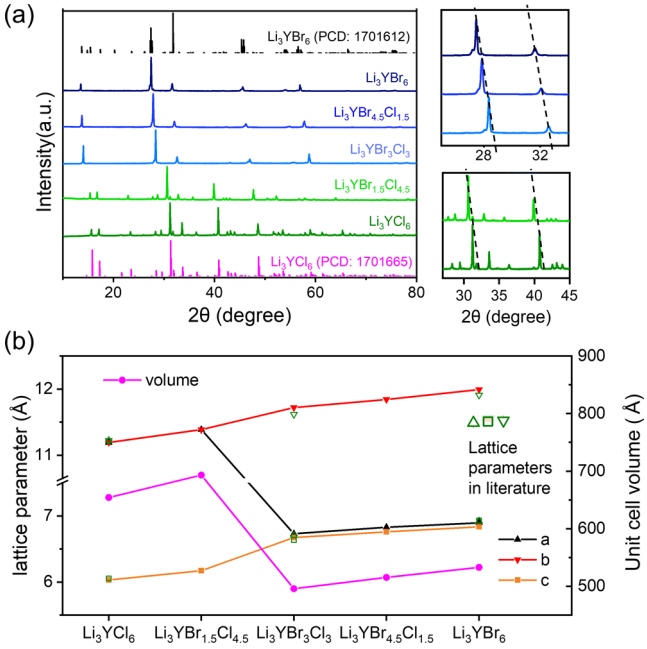

Figure 1. (a) X-ray diffraction patterns of the series of $Li_3YBr_xCl_{6-x}$ (x = 0−6) solid electrolytes. Magnified images of a group of characteristic peaks from the diffraction patterns of the $Li_3YBr_xCl_{6-x}$ samples are shown. (b) Evolution of the lattice parameters of $Li_3YBr_xCl_{6-x}$ as a function of x as obtained from the Le Bail refinement of the X-ray diffraction data. For comparison, the lattice parameters of each halide achieved from previous reports are shown (Li_3YBr_6/Cl_6 from ref 2, $Li_3YBr_3Cl_3$ from ref 10).

The Li_3YCl_6 sample crystallized in the trigonal $P\bar{3}m1$ (#164)[24] space group, as does $Li_3YBr_xCl_{6-x}$ with x = 1.5. The materials with x > 1.5, as well as the full bromide Li_3YBr_6, crystallize in monoclinic $C2/m$ (#12)[25] space group. Due to the larger anion radius of Br, the lattice parameters increase as Br is added to the system (Figure 1b). Between the compositions $Li_3YBr_xCl_{6-x}$, x = 1.5 and x = 3, where the phase transition occurs, the volume of the unit cell decreases due to the smaller unit cell size of the monoclinic phase. The volume per chemical formula unit increases linearly with bromine content (SI Figure S1). With conventional Rietveld refinement, it was not possible to refine the X-ray data due to mismatch in peak intensities, especially the peaks between 2θ = 18−25° for the $C2/m$ phase. To investigate this effect, different synthesis methods were applied (mechanochemical synthesis, mechanochemical synthesis + annealing step, co-melting) comparing the resulting morphology and diffraction patterns (SI Figures 2 and S3 and Text 1). While mechanochemical synthesis leads to a fine powder with no distinct features in the

https://doi.org/10.1021/acs.jpcc.2c07910
J. Phys. Chem. C XXXX, XXX, XXX−XXX

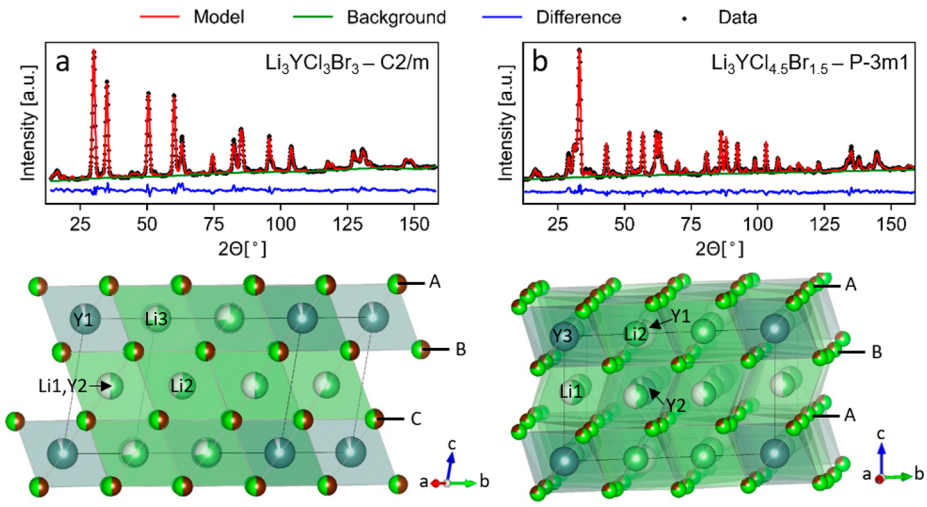

Figure 2. Rietveld refinement of the neutron diffraction data (top) and crystal structure (bottom) for the monoclinic (a) and trigonal (b) phase of $Li_3YBr_xCl_{6-x}$. (a) Structure solution of $Li_3YBr_xCl_{6-x}$ for x = 3 The cubic close packing-like framework is highlighted along the c-direction, as illustrated by the alternating layers A, B, and C. The Y atoms mostly occupy the Y1 (2a) site, with some on the Y2(4h) site. The 4h site is shared with Li. The lithium is distributed across the 4h site and the other empty octahedra. (b) Structure solution for $Li_3YBr_xCl_{6-x}$ for x = 1.5. The hexagonal close packing like framework is along the c-direction, as indicated by the alternating A and B layers. There is one fully occupied Y site, i.e., Y3(1a). The Y2(2d) site is almost fully occupied, while the Y1(2d) site is only 7% occupied.

microstructure, heat treatment above 500 °C leads to the formation of platelets (SI Figure 4), which corresponds to the disappearance of the Bragg peaks between 2θ = 18−25° (SI Figure 2). This suggests that the anisotropic, platelet-like morphology, which can show as preferred orientation due to nonrandom orientation of the powder when the X-ray diffraction data is measured in Bragg−Brentano geometry, could be at least a source of the discrepancy. However, recent literature has reported the occurrence of stacking faults in Li_3YCl_6[26] and $Li_3HoBr_xI_{6-x}$,[8] presenting an alternative origin for the discrepancy (SI Text 1). As described in ref 26, neutron diffraction data are less sensitive to stacking faults compared to X-ray diffraction in Li_3YCl_6, due to the different contrast. Further, due to the larger amount of sample and the transmission geometry, the neutron diffraction data are also less sensitive to preferred orientation, compared to X-ray diffraction data measured in Bragg−Brentano geometry. Therefore, neutron diffraction was performed to confirm the monoclinic average symmetry and to learn more about the structural effect of anion substitution in $Li_3YBr_xCl_{6-x}$ by means of Rietveld refinement (Figure 2a,b, SI Figures S5−S14 including visual models, and SI Tables S1−S5).

The crystal structures of the trigonal and monoclinic phases have distinct structural characteristics (Figure 2). The trigonal structure with the compositions $Li_3YBr_xCl_{6-x}$ at x = 0 and 1.5 is built by hexagonal close-packing (hcp)-like arrangement of the halogen atoms, with the Y and Li in octahedral positions. The Rietveld refinement shows that the Cl and Br atoms distribute statistically across the halogen sites (as consistent with literature; see refs 8−10) and small differences in the Y and Li occupancies (SI Tables S4 and S5). The monoclinic phase with the compositions $Li_3YBr_xCl_{6-x}$ at x = 3, 4.5, and 6 on the other hand, shows cubic close packing (ccp) of the halogen atoms. Similar to the trigonal phase, the Cl and Br distribute statistically across the halogen sites and the Y and Li reside on octahedral sites. Also here, there appear to be small redistributions of the Li and Y, but there is no clear trend as a function of x (SI Tables S1−S3). No tetrahedral sites were necessary for a physically consistent refinement as reported in isostructural chlorides.[27,28] Despite that the tetrahedral voids are not occupied on average, they are still available as interstitial sites for the diffusion pathways.

The ionic conductivities of the various $Li_3YBr_xCl_{6-x}$ solid electrolytes as a function of temperature are determined by broadband AC impedance spectroscopy (Figure 3; for fits of

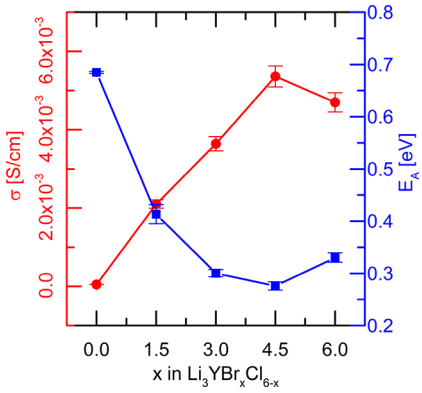

Figure 3. Ionic conductivity σ [S/cm] at 30 °C and activation energies extracted from the Arrhenius relationship (see SI Figures S15−S19) of $Li_3YBr_xCl_{6-x}$.

individual measurements and validation of the circuit model by the Kramers−Kronig relationship, see supplementary files). The ionic conductivity at 30 °C is lowest for Li_3YCl_6 at 0.05 × 10^{-3} S/cm. Already the small amount of Br in $Li_3YBr_{1.5}Cl_{4.5}$ leads to a large increase in ionic conductivity to 2.1 × 10^{-3} S/cm, where the material is still in the trigonal phase. The ionic conductivity increases further as x is increased and reaches a maximum of 5.36 × 10^{-3} S/cm for $Li_3YBr_{4.5}Cl_{1.5}$ in the monoclinic phase. The activation energy reflects a similar trend: it has the highest value for the chloride end-member Li_3YCl_6 (0.685 eV), reduces to 0.413 eV for $Li_3YBr_{1.5}Cl_{4.5}$, and reaches its minimum of 0.276 eV for $Li_3YBr_{4.5}Cl_{1.5}$ (Figure 3; see SI Figures S15−S19 for the complete conductivity datasets

https://doi.org/10.1021/acs.jpcc.2c07910
J. Phys. Chem. C XXXX, XXX, XXX−XXX

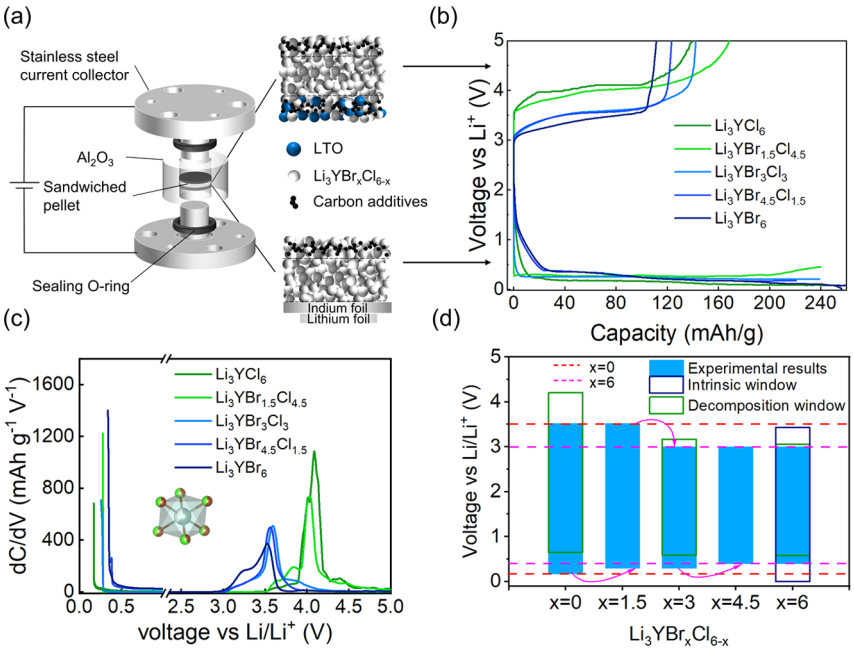

Figure 4. Electrochemical stability assessment in ASSBs with $Li_3YBr_xCl_{6-x}$ (a) Schematic view of the cell configuration. Different configurations of pellets are pressed between the blocking electrodes. Carbon and $Li_3YBr_xCl_{6-x}$ composites are used as working electrodes, while $Li_4Ti_5O_{12}$ (LTO)-C and In−Li are used as counter electrodes, respectively. (b) Galvanostatic charge and discharge curves of $Li_3YBr_xCl_{6-x}$-C|$Li_3YBr_xCl_{6-x}$|LTO-C and $Li_3YBr_xCl_{6-x}$-C|$Li_3YBr_xCl_{6-x}$|In−Li ASSBs, respectively. (c) Differential capacity dC/dV curves of the redox activities of $Li_3YBr_xCl_{6-x}$ solid electrolytes. (d) Electrochemical stability window inferred from the experimental voltage profiles. The dashed lines indicate the redox potential barriers of Li_3YCl_6 and Li_3YBr_6, and the arrows indicate where the barriers shift within the $Li_3YBr_xCl_{6-x}$ solid electrolytes. The thermodynamic decomposition windows[14] and intrinsic windows predicted based on DFT calculation[16] are also plotted for comparison. The thermodynamic decomposition window is the voltage at which the material decomposes to the most stable known products, whereas the intrinsic window represents the voltage at which the solid electrolytes de/lithiate, allowing the formation of reaction intermediates.

and Arrhenius relationship fits). There are many reasons that could cause differences in ionic conductivities in this substitution series:

- The association energy of Li with Br is smaller than that with Cl, due to the smaller electronegativity/larger lattice polarizability.[29−31]
- As the crystal structure transitions from the trigonal to the monoclinic phase, the anionic framework transforms from hexagonal close packing (hcp) to cubic close packing (ccp). In the hexagonal close packing, lithium can jump through face-sharing octahedral−octahedral (oct−oct), octahedral−tetrahedral−octahedral (oct−tet−oct), and tetrahedral−tetrahedral (tet−tet) pathways. In the cubic close packed framework, only oct−tet−oct paths exist.[32] Calculations have shown that hcp chlorides have slightly lower activation energies (0.25 eV oct−oct and 0.29 oct−tet−oct) compared to ccp bromides (0.28 oct−tet−oct).[14]
- With the introduction of more (larger) Br, the lattice expands, rendering larger polyhedral faces ("bottlenecks") for the Li to jump through.[33,34]
- (Small) changes in the Y and/or Li site occupancies may affect the ionic conductivity.[35,36]
- Finally, there are reports that the increase in configurational entropy in mixed (poly)anion substituted samples may alter the ionic conductivity.[37,38]

While it is not possible to deconvolute these factors based on the data presented here, some general observations can be made. First of all, if the increase in ionic conductivity due to the larger lattice polarizability was the only/main factor at play, the activation energy should decrease monotonically with x, which is not the case. A similar argument can be made for the configurational entropy, if it was the only/main factor at play the maximum in ionic conductivity should be found at $x = 3$ in $Li_3YBr_xCl_{6-x}$. The trigonal phase has much higher activation energies (0.685 eV for $x = 0$, 0.413 eV for $x = 1.5$) compared to the monoclinic phase (0.300 eV for $x = 3$, 0.276 eV for $x = 4.5$, 0.330 eV for $x = 6$), it is therefore rather likely that the ccp-like packing is more favorable, as also postulated theoretically in literature for sulfides (where, however, Li preferentially resides in tetrahedral coordination).[32] Considering the large change in ionic conductivity from Li_3YCl_6 to $Li_3YBr_{1.5}Cl_{4.5}$, it is likely that the increase of the lattice parameters aids the conductivity in the $P\bar{3}m1$ phase. To investigate the effect of site occupancies, more compositions should be considered and X-ray diffraction data should be refined simultaneously with the neutron diffraction data for more accurate site occupancies. The deconvolution of these different effects and determination of detailed site occupancies are subject of future research.

Experimentally measuring the solid electrolyte stability window is challenging. Previous reports have often determined the electrochemical stability window using cyclic voltammetry (CV), which shows a pair of peaks to reflect the reduction and oxidation reactions.[10,39,40] However, the short exposure time of a CV scan makes it challenging to probe the electrochemical stability window of solid electrolytes, in which the kinetics of decomposition are sluggish due to the limited contact area, poor electronic conductivity, and charge transfer.[15] To circumvent these problems, the electrochemical stability was measured as reported in Schwietert et al.[15] Electrochemical

https://doi.org/10.1021/acs.jpcc.2c07910
J. Phys. Chem. C XXXX, XXX, XXX−XXX

cells were assembled using a simultaneous reference and counter electrode (in this case a Li intercalation ($Li_4Ti_5O_{12}$ (LTO-C)) and alloying compound (Li−In) with constant potential for the Li concentrations measured) and a composite of the solid electrolyte mixed with carbon black as a working electrode (see schematic Figure 4a). The composite was then oxidized and reduced using galvanostatic measurements at 6.5 $\mu A/cm^2$, so that the oxidation and reduction potential could be measured with minimal overpotential. The voltage curve of these cells is shown in Figure 4b. The curves show clear plateaus with large specific capacities (100−240 mAh/g of solid electrolyte), indicating that there is significant oxidation and reduction of the solid electrolytes.

The onset of the voltage plateaus corresponds to the onset voltages of the peaks in the differential capacity curves (Figure 4c). This onset voltage is where decomposition is initiated, and is the limiting value used for the decomposition window that is plotted in Figure 4d. The plot shows that the oxidative stability of $Li_3YBr_xCl_{6-x}$ can be split into two groups, one with an oxidation onset at 3.0 V for $3 < x \leq 6$ and 3.5 V for $x \leq 3$. This two groups can be distinguished in two ways, namely their crystal structure ($P\bar{3}m1$ vs $C2/m$), as well as the dominant anion (Cl-rich vs Br-rich). Oxidation of the halogen would, according to thermodynamic calculations, lead to the formation of halogen gas. Therefore, two Br atoms would need to be in close proximity to each other. Low enough Br concentrations could ensure that the Br are enough separate in space that the necessity for to Br atoms in close proximity is not given and oxidation cannot happen. On the other hand, it could also be due to the trigonal crystal structure (or the hcp-like arrangement of the anions) which could be less prone to oxidize compared to the monoclinic structure (or ccp-like arrangement of the anions).

For Li_3YBr_6, the oxidation onset value from the dC/dV curve is at 3 V which is smaller than the calculated thermodynamic decomposition window (3.15 V) and the intrinsic (oxidation and reduction) window (3.43 V). For Li_3YCl_6, the oxidation onset at 3.5 V is also smaller compared to the calculated thermodynamic decomposition window (4.21 V).

It is interesting to consider the position of the maxima of the dC/dV curves, as in principle it could be more representative of bulk values, should interface effects lower the onset potential. For Li_3YBr_6, the maximum of the dC/dV curve is at 3.4 V, which corresponds with the voltage predicted by the calculations of the intrinsic window. For Li_3YCl_6, the maximum of the dC/dV curve is at 4.2 V, the value predicted for the thermodynamic decomposition window.

To conclude, the experimental data confirm the trend in oxidation potential predicted by theoretical calculations between Li_3YBr_6 and Li_3YCl_6, but neither calculation method accurately predicts the values observed here.

Considering the mixed halide samples $Li_3YBr_xCl_{6-x}$ (x = 1.5, 3, 4.5), there is a clear trend. Low Br concentrations do not affect the oxidation potential, as trigonal $Li_3YBr_{1.5}Cl_{4.5}$ follows the behavior of the trigonal chloride end-member Li_3YCl_6. All other compositions, crystallizing in the monoclinic phase, $Li_3YBr_xCl_{6-x}$ (x = 3, 4.5) show similar behavior to monoclinic bromide end-member Li_3YBr_6 (see Figure 4d).

The electrolytes $Li_3YBr_xCl_{6-x}$ (x = 1.5, 4.5) were tested in full cells using single crystal NCM811/halide SE composite as cathode, halide SE as electrolyte, a Li_6PS_5Cl interlayer, and Li−In as anode (see Figure S20). $Li_3YBr_xCl_{6-x}$ with x = 1.5 showed a first cycle Coulombic efficiency of 79.95%, compared to 73.05% for x = 4.5 (in comparison, the same cathode tested in a liquid cell had 83.79% Coulombic efficiency). This is an indicator for less SE decomposition during the first cycle.

Concluding, results of the ionic conductivity and electrochemical window measurements show that there is a trade-off in the $Li_3YBr_xCl_{6-x}$ substitution range. While the ionic conductivity is highest at x = 4.5 in the monoclinic phase, the electrolyte starts to oxidize at 3 V, similar to Li_3YBr_6. Small Br concentrations, here represented by x = 1.5, increase the ionic conductivity significantly in the $P\bar{3}m1$ phase but maintain the high oxidation potential of Li_3YCl_6.

■ CONCLUSIONS

The substitution series $Li_3YBr_xCl_{6-x}$ (x = 0, 1.5, 3, 4.5, 6) were synthesized by co-melting of the precursors. The proposed crystal structures (trigonal $P\bar{3}m1$/monoclinic $C2/m$) for Li_3YCl_6/Li_3YBr_6 are a good fit to neutron diffraction data as demonstrated by Rietveld refinement. The composition $Li_3YCl_{4.5}Br_{1.5}$ crystallized in trigonal $P\bar{3}m1$ (like Li_3YCl_6), and the compositions $Li_3YBr_xCl_{6-x}$ with x = 3, 4.5 in monoclinic $C2/m$ (like Li_3YBr_6),

Already a small Br content (x = 1.5) increases the ionic conductivity by 2 orders of magnitude compared to Li_3YCl_6 (2.02 compared to 0.047 × 10^{-3} S/cm at 30 °C). The maximum ionic conductivity of 5.18 × 10^{-3} S/cm at 30 °C is reached for the monoclinic $Li_3Ybr_xCl_{6-x}$ with x = 4.5. The investigation of the oxidative stability confirm that the solid electrolytes with high Cl content have a higher oxidation potential compared to the ones with high Br content. A small amount of Br substitution (x = 1.5) does not affect the oxidation potential and the measurement shows similar behavior to stable Li_3YCl_6, whereas larger Br contents (x = 3, 4.5) show behavior similar to the less electrochemically stable Li_3YBr_6. These results show a clear trade-off between ionic conductivity and electrochemical stability in this substitution series.

We highlight the lightly Br-substituted $Li_3YCl_{4.5}Br_{1.5}$ as the best compromise, achieving the "best of both end-members", with a conductivity ∼200 higher than trigonal Li_3YCl_6 and an oxidative stability ∼0.5 V higher than monoclinic Li_3YBr_6. This work highlights that careful optimization of composition and substitutions in the anion framework provide prolific and rational avenues for designing the properties of future solid electrolytes.

■ ASSOCIATED CONTENT

Supporting Information

The Supporting Information is available free of charge at https://pubs.acs.org/doi/10.1021/acs.jpcc.2c07910.

Dependence of the synthesis method on X-ray diffraction pattern and microstructure; relationship volume per formula unit vs Br/Cl ratio; Rietveld refinement of neutron diffraction data, corresponding structure solution and visualized crystal structure for $Li_3YBr_xCl_{6-x}$ (x = 0, 1.5, 3, 4.5, 6); Arrhenius relationship obtained from AC impedance measurements for $Li_3YBr_xCl_{6-x}$ (x = 0, 1.5, 3, 4.5, 6); battery performance using electrolytes $Li_3YBr_xCl_{6-x}$ (x = 1.5, 4.5) (PDF)

Reports to the equivalent circuit fits of the impedance spectra of $Li_3YCl_3Br_3$ (PDF)

https://doi.org/10.1021/acs.jpcc.2c07910
J. Phys. Chem. C XXXX, XXX, XXX−XXX

Reports to the equivalent circuit fits of the impedance spectra of Li_3YBr_6 (PDF)

Reports to the equivalent circuit fits of the impedance spectra of Li_3YCl_6 (PDF)

Reports to the equivalent circuit fits of the impedance spectra of $Li_3YCl_{15}Br_{45}$ (PDF)

Reports to the equivalent circuit fits of the impedance spectra of $Li_3YCl_{45}Br_{15}$ (PDF)

Kramers–Kronig analysis of Li_3YBr_6 (PDF)

Kramers–Kronig analysis of $Li_3YCl_3Br_3$ (PDF)

Kramers–Kronig analysis of Li_3YCl_6 (PDF)

Kramers–Kronig analysis of $Li_3YCl_{15}Br_{45}$ (PDF)

Kramers–Kronig analysis of $Li_3YCl_{45}Br_{15}$ (PDF)

AUTHOR INFORMATION

Corresponding Authors

Swapna Ganapathy – *Department of Radiation Science and Technology, Faculty of Applied Sciences, Delft University of Technology, 2629JB Delft, The Netherlands;* orcid.org/0000-0001-5265-1663; Email: s.ganapathy@tudelft.nl

Marnix Wagemaker – *Department of Radiation Science and Technology, Faculty of Applied Sciences, Delft University of Technology, 2629JB Delft, The Netherlands;* orcid.org/0000-0003-3851-1044; Email: m.wagemaker@tudelft.nl

Authors

Eveline van der Maas – *Department of Radiation Science and Technology, Faculty of Applied Sciences, Delft University of Technology, 2629JB Delft, The Netherlands;* orcid.org/0000-0003-3610-7283

Wenxuan Zhao – *Department of Radiation Science and Technology, Faculty of Applied Sciences, Delft University of Technology, 2629JB Delft, The Netherlands*

Zhu Cheng – *Department of Radiation Science and Technology, Faculty of Applied Sciences, Delft University of Technology, 2629JB Delft, The Netherlands*

Theodosios Famprikis – *Department of Radiation Science and Technology, Faculty of Applied Sciences, Delft University of Technology, 2629JB Delft, The Netherlands;* orcid.org/0000-0002-7946-1445

Michel Thijs – *Department of Radiation Science and Technology, Faculty of Applied Sciences, Delft University of Technology, 2629JB Delft, The Netherlands*

Steven R. Parnell – *Department of Radiation Science and Technology, Faculty of Applied Sciences, Delft University of Technology, 2629JB Delft, The Netherlands*

Complete contact information is available at: https://pubs.acs.org/10.1021/acs.jpcc.2c07910

Author Contributions

[†]E.vdM. and W.Z. contributed equally.

Notes

The authors declare no competing financial interest.

ACKNOWLEDGMENTS

Financial support was provided by the "Nederlandse organisatie voor Wetenschappelijk Onderzoek" (NWO), VICI Grant Number 16122 for M.W. T. F. acknowledges funding from the European Union, in the form of a Marie Skłodowska-Curie individual postdoctoral fellowship (project no. 101066486).

REFERENCES

(1) Famprikis, T.; Canepa, P.; Dawson, J. A.; Islam, M. S.; Masquelier, C. Fundamentals of Inorganic Solid-State Electrolytes for Batteries. *Nat. Mater.* **2019**, *18*, 1278–1291.

(2) Asano, T.; Sakai, A.; Ouchi, S.; Sakaida, M.; Miyazaki, A.; Hasegawa, S. Solid Halide Electrolytes with High Lithium-Ion Conductivity for Application in 4 V Class Bulk-Type All-Solid-State Batteries. *Adv. Mater.* **2018**, *30* (44), 1803075.

(3) Li, X.; Liang, J.; Yang, X.; Adair, K. R.; Wang, C.; Zhao, F.; Sun, X. Progress and Perspectives of Halide-Based Lithium Conductors for All-Solid-State Batteries. *Energy Environ. Sci.* **2020**, *13*, 1429–1461.

(4) Wang, C.; Liang, J.; Kim, J. T.; Sun, X. Prospects of Halide-Based All-Solid-State Batteries: From Material Design to Practical Application. *Sci. Adv.* **2022**, *8* (36), eadc9516.

(5) Zhang, Q.; Gao, Z.; Shi, X.; Zhang, C.; Liu, K.; Zhang, J.; Zhou, L.; Ma, C.; Du, Y. Recent Advances on Rare Earths in Solid Lithium Ion Conductors. *J. Rare Earths* **2021**, *39* (1), 1–10.

(6) Kwak, H.; Wang, S.; Park, J.; Liu, Y.; Kim, K. T.; Choi, Y.; Mo, Y.; Jung, Y. S. Emerging Halide Superionic Conductors for All-Solid-State Batteries: Design, Synthesis, and Practical Applications. *ACS Energy Lett.* **2022**, *7* (5), 1776–1805.

(7) Zhou, L.; Zuo, T.-T.; Kwok, C. Y.; Kim, S. Y.; Assoud, A.; Zhang, Q.; Janek, J.; Nazar, L. F. High Areal Capacity, Long Cycle Life 4 V Ceramic All-Solid-State Li-Ion Batteries Enabled by Chloride Solid Electrolytes. *Nat. Energy* **2022**, *7*, 83–93.

(8) Plass, M. A.; Bette, S.; Dinnebier, R. E.; Lotsch, B. V. Enhancement of Superionic Conductivity by Halide Substitution in Strongly Stacking Faulted $Li_3HoBr_{6-x}I_x$ Phases. *Chem. Mater.* **2022**, *34* (7), 3227–3235.

(9) Bohnsack, A.; Meyer, G. Ternäre Halogenide vom Typ A_3MX_6. V. Synthese, Kristallstrukturen und Natrium-Ionenleitfähigkeit der ternären Iodide Na_3MI_6 (M = Sm, Gd-Dy) sowie der Mischkristalle $Na_3GdBr_{6-x}I_x$. *Z. Für Anorg. Allg. Chem.* **1997**, *623* (1–6), 837–843.

(10) Liu, Z.; Ma, S.; Liu, J.; Xiong, S.; Ma, Y.; Chen, H. High Ionic Conductivity Achieved in $Li_3Y(Br_3Cl_3)$ Mixed Halide Solid Electrolyte via Promoted Diffusion Pathways and Enhanced Grain Boundary. *ACS Energy Lett.* **2021**, *6* (1), 298–304.

(11) Tomita, Y.; Matsushita, H.; Kobayashi, K.; Maeda, Y.; Yamada, K. Substitution Effect of Ionic Conductivity in Lithium Ion Conductor, $Li_3InBr_{6-x}Cl_x$. *Solid State Ion.* **2008**, *179* (21–26), 867–870.

(12) Tomita, Y.; Nishiyama, H.; Kobayashi, K.; Kohno, Y.; Maeda, Y.; Yamada, K. Substitution Effect for Br on the Lithium Ion Conductivity of Lithium Indium Bromide. *ECS Trans.* **2009**, *16*, 137–141.

(13) Zevgolis, A.; Wood, B. C.; Mehmedović, Z.; Hall, A. T.; Alves, T. C.; Adelstein, N. Alloying Effects on Superionic Conductivity in Lithium Indium Halides for All-Solid-State Batteries. *APL Mater.* **2018**, *6* (4), 047903.

(14) Wang, S.; Bai, Q.; Nolan, A. M.; Liu, Y.; Gong, S.; Sun, Q.; Mo, Y. Lithium Chlorides and Bromides as Promising Solid-State Chemistries for Fast Ion Conductors with Good Electrochemical Stability. *Angew. Chem., Int. Ed.* **2019**, *58* (24), 8039–8043.

(15) Schwietert, T. K.; Arszelewska, V. A.; Wang, C.; Yu, C.; Vasileiadis, A.; de Klerk, N. J. J.; Hageman, J.; Hupfer, T.; Kerkamm, I.; Xu, Y.; et al. Clarifying the Relationship between Redox Activity and Electrochemical Stability in Solid Electrolytes. *Nat. Mater.* **2020**, *19* (4), 428–435.

(16) Schwietert, T. K.; Vasileiadis, A.; Wagemaker, M. First-Principles Prediction of the Electrochemical Stability and Reaction Mechanisms of Solid-State Electrolytes. *JACS Au* **2021**, *1* (9), 1488–1496.

(17) Park, D.; Park, H.; Lee, Y.; Kim, S.-O.; Jung, H.-G.; Chung, K. Y.; Shim, J. H.; Yu, S. Theoretical Design of Lithium Chloride Superionic Conductors for All-Solid-State High-Voltage Lithium-Ion Batteries. *ACS Appl. Mater. Interfaces* **2020**, *12* (31), 34806–34814.

(18) Kochetkov, I.; Zuo, T.-T.; Ruess, R.; Singh, B.; Zhou, L.; Kaup, K.; Janek, J.; Nazar, L. Different Interfacial Reactivity of Lithium Metal Chloride Electrolytes with High Voltage Cathodes Determines

Solid-State Battery Performance. *Energy Environ. Sci.* **2022**, *15*, 3933−3944.
(19) Toby, B. H.; Von Dreele, R. B. *GSAS-II*: The Genesis of a Modern Open-Source All Purpose Crystallography Software Package. *J. Appl. Crystallogr.* **2013**, *46* (2), 544−549.
(20) Toby, B. H.; Von Dreele, R. B. What's New in GSAS-II. *Powder Diffr.* **2014**, *29* (S2), S2−S6.
(21) van Eijck, L.; Cussen, L. D.; Sykora, G. J.; Schooneveld, E. M.; Rhodes, N. J.; van Well, A. A.; Pappas, C. Design and performance of a novel neutron powder diffractometer: PEARL at TU Delft. *J. Appl. Crystallogr.* **2016**, *49*, 1398−1401.
(22) Momma, K.; Izumi, F. *VESTA*: A Three-Dimensional Visualization System for Electronic and Structural Analysis. *J. Appl. Crystallogr.* **2008**, *41* (3), 653−658.
(23) Krasnikova, I. V.; Pogosova, M. A.; Sanin, A. O.; Stevenson, K. J. Toward Standardization of Electrochemical Impedance Spectroscopy Studies of Li-Ion Conductive Ceramics. *Chem. Mater.* **2020**, *32* (6), 2232−2241.
(24) Bohnsack, A.; Stenzel, F.; Zajonc, A.; Balzer, G.; Wickleder, M. S.; Meyer, G. Ternäre Halogenide vom Typ A_3MX_6. VI [1]. Ternäre Chloride der Selten-Erd-Elemente mit Lithium, Li_3MCl_6 (M = Tb-Lu, Y, Sc): Synthese, Kristallstrukturen und Ionenbewegung. *Z. Für Anorg. Allg. Chem.* **1997**, *623* (7), 1067−1073.
(25) Bohnsack, A.; Balzer, G.; Gödel, H.-U.; Wickleder, M. S.; Meyer, G. Ternäre Halogenide vom Typ A_3MX_6. VII [1]. Die Bromide Li_3MBr_6 (M = Sm-Lu, Y): Synthese, Kristallstruktur, Ionenbeweglichkeit. *Z. Für Anorg. Allg. Chem.* **1997**, *623* (9), 1352−1356.
(26) Sebti, E.; Evans, H. A.; Chen, H.; Richardson, P. M.; White, K. M.; Giovine, R.; Koirala, K. P.; Xu, Y.; Gonzalez-Correa, E.; Wang, C.; et al. Stacking Faults Assist Lithium-Ion Conduction in a Halide-Based Superionic Conductor. *J. Am. Chem. Soc.* **2022**, *144* (13), 5795−5811.
(27) Helm, B.; Schlem, R.; Wankmiller, B.; Banik, A.; Gautam, A.; Ruhl, J.; Li, C.; Hansen, M. R.; Zeier, W. G. Exploring Aliovalent Substitutions in the Lithium Halide Superionic Conductor $Li_{3-x}In_{1-x}Zr_xCl_6$ ($0 \leq x \leq 0.5$). *Chem. Mater.* **2021**, *33* (12), 4773−4782.
(28) Kwak, H.; Han, D.; Son, J. P.; Kim, J. S.; Park, J.; Nam, K.-W.; Kim, H.; Jung, Y. S. Li+ Conduction in Aliovalent-Substituted Monoclinic Li_2ZrCl_6 for All-Solid-State Batteries: $Li_{2+x}Zr_{1-X}M_xCl_6$ (M = In, Sc). *Chem. Eng. J.* **2022**, *437*, 135413.
(29) Muy, S.; Schlem, R.; Shao-Horn, Y.; Zeier, W. G. Phonon−Ion Interactions: Designing Ion Mobility Based on Lattice Dynamics. *Adv. Energy Mater.* **2021**, *11* (15), 2002787.
(30) Kraft, M. A.; Culver, S. P.; Calderon, M.; Böcher, F.; Krauskopf, T.; Senyshyn, A.; Dietrich, C.; Zevalkink, A.; Janek, J.; Zeier, W. G. Influence of Lattice Polarizability on the Ionic Conductivity in the Lithium Superionic Argyrodites Li_6PS_5X (X = Cl, Br, I). *J. Am. Chem. Soc.* **2017**, *139* (31), 10909−10918.
(31) Schlem, R.; Bernges, T.; Li, C.; Kraft, M. A.; Minafra, N.; Zeier, W. G. Lattice Dynamical Approach for Finding the Lithium Superionic Conductor Li_3ErI_6. *ACS Appl. Energy Mater.* **2020**, *3* (4), 3684−3691.
(32) Wang, Y.; Richards, W. D.; Ong, S. P.; Miara, L. J.; Kim, J. C.; Mo, Y.; Ceder, G. Design Principles for Solid-State Lithium Superionic Conductors. *Nat. Mater.* **2015**, *14* (10), 1026−1031.
(33) Ohno, S.; Banik, A.; Dewald, G. F.; Kraft, M. A.; Krauskopf, T.; Minafra, N.; Till, P.; Weiss, M.; Zeier, W. G. Materials Design of Ionic Conductors for Solid State Batteries. *Prog. Energy* **2020**, *2* (2), 022001.
(34) Martínez-Juárez, A.; Pecharromán, C.; Iglesias, J. E.; Rojo, J. M. Relationship between Activation Energy and Bottleneck Size for Li^+ Ion Conduction in NASICON Materials of Composition $LiMM'(PO_4)_3$; M, M' = Ge, Ti, Sn, Hf. *J. Phys. Chem. B* **1998**, *102* (2), 372−375.
(35) Schlem, R.; Muy, S.; Prinz, N.; Banik, A.; Shao-Horn, Y.; Zobel, M.; Zeier, W. G. Mechanochemical Synthesis: A Tool to Tune Cation Site Disorder and Ionic Transport Properties of Li_3MCl_6 (M = Y, Er) Superionic Conductors. *Adv. Energy Mater.* **2020**, *10* (6), 1903719.
(36) Schlem, R.; Banik, A.; Ohno, S.; Suard, E.; Zeier, W. G. Insights into the Lithium Substructure of the Superionic Conductors Li_3YCl_6 and Li_3YBr_6. 27. *Chem. Mater.* **2021**, *33*, 327−337.
(37) Strauss, F.; Lin, J.; Duffiet, M.; Wang, K.; Zinkevich, T.; Hansen, A.-L.; Indris, S.; Brezesinski, T. High-Entropy Polyanionic Lithium Superionic Conductors. *ACS Mater. Lett.* **2022**, *4* (2), 418−423.
(38) Deng, Y.; Eames, C.; Fleutot, B.; David, R.; Chotard, J.-N.; Suard, E.; Masquelier, C.; Islam, M. S. Enhancing the Lithium Ion Conductivity in Lithium Superionic Conductor (LISICON) Solid Electrolytes through a Mixed Polyanion Effect. *ACS Appl. Mater. Interfaces* **2017**, *9* (8), 7050−7058.
(39) Liang, J.; Maas, E.; Luo, J.; Li, X.; Chen, N.; Adair, K. R.; Li, W.; Li, J.; Hu, Y.; Liu, J.; et al. New Series of Ternary Metal Chloride Superionic Conductors for High Performance All-Solid-State Lithium Batteries. *Adv. Energy Mater.* **2022**, *12*, 2103921.
(40) Liang, J.; Li, X.; Wang, S.; Adair, K. R.; Li, W.; Zhao, Y.; Wang, C.; Hu, Y.; Zhang, L.; Zhao, S.; et al. Site-Occupation-Tuned Superionic Li_xScCl_{3+x} Halide Solid Electrolytes for All-Solid-State Batteries. *J. Am. Chem. Soc.* **2020**, *142* (15), 7012−7022.

■ NOTE ADDED AFTER ASAP PUBLICATION

This paper was published on December 16, 2022. Two numbers were transposed near the end of the Results and Discussion section. The corrected version was reposted on December 16, 2022.

https://doi.org/10.1021/acs.jpcc.2c07910
J. Phys. Chem. C XXXX, XXX, XXX−XXX